RESEARCH ARTICLE

Biases of five latent heat flux products and their impacts on mixed-layer temperature estimates in the South China Sea

Xin Wang[1,2] (iD), Rongwang Zhang[3] (iD), Jian Huang[4] (iD), Lili Zeng[1] (iD), and Fei Huang[3,4]

[1]State Key Laboratory of Tropical Oceanography, South China Sea Institute of Oceanology, Chinese Academy of Sciences, Guangzhou, China, [2]Laboratory for Regional Oceanography and Numerical Modeling, Qingdao National Laboratory of Marine Science and Technology, Qingdao, China, [3]Physical Oceanography Laboratory/CIMST, Ocean University of China and Qingdao National Laboratory for Marine Science and Technology, Qingdao, China, [4]Joint Open Laboratory of Marine Meteorology, Guangzhou Institute of Tropical and Marine Meteorology, China Meteorological Administration, Guangzhou, China

Abstract Five latent heat flux (LHF) products are evaluated based on in situ observations in the South China Sea (SCS), including the ECWMF ERA-Interim (ERA-I), the NCEP2, the Objectively Analyzed air-sea Fluxes (OAFlux), the Japanese 55 year Reanalysis (JRA55), and the TropFlux data sets. The results show that there are good correlations between the LHF products and observations, ranging from 0.68 to 0.74. However, mean biases of -8 to 40 W m^{-2} exist in the LHF products with respect to the observations. For root-mean-square errors, the OAFlux data set is the closest to the observations, followed by ERA-I and TropFlux, while the NCEP2 data set shows significant overestimation. It is found that the biases in the near-surface-specific humidity are most correlated with the biases in the LHF products, followed by the biases in the near-surface wind speed, air temperature, and sea surface temperature. The biases in the LHF products have a prominent seasonal variation that is 25 W m^{-2} higher in boreal winter than in summer. Using the thermal equation, it is shown that the tendency errors of the mixed-layer temperature estimated by the biases in the LHF products vary from -2.0 to 3.5°C/month in the SCS. When all of the products are averaged, the errors are reduced to a range of -0.7 to 1.5°C/month. It is noteworthy that the errors in summer are more obvious than those in winter, since a thinner mixed layer in the summer can amplify the effect of even a small bias in the LHF.

1. Introduction

Turbulent fluxes between the ocean and atmosphere, including heat fluxes and momentum flux, can affect the structure of the atmospheric boundary layer and the upper ocean, thereby modulating both atmospheric circulation and ocean circulation. These fluxes are specified as boundary conditions for ocean and climate models and have nonnegligible effects on model performance [*Chou et al.*, 2004; *Chaudhuri et al.*, 2013]. The heat fluxes contain four components: shortwave radiation (SWR) flux, longwave radiation (LWR) flux, latent heat flux (LHF), and sensible heat flux (SHF). Their sum is the net heat flux (Q_{net}). It is known that the SWR and LHF contribute the most to the Q_{net}. Though the magnitude of the LHF is smaller than the SWR, it has a larger spatiotemporal variation [*Chou et al.*, 2003; *Kubota et al.*, 2003]. In addition, the LHF links the heat and hydrological transports between the ocean and atmosphere [*Grodsky et al.*, 2009], a dynamic which has been widely studied in recent years [*Schulz et al.*, 1997; *Kubota et al.*, 2003; *Chou et al.*, 2004; *Singh et al.*, 2005; *Bourras*, 2006; *Liu et al.*, 2011].

LHF products are provided by a variety of reanalysis data sets, which can be global, gridded and near-real time. However, differences exist among these products due to the different data assimilation and/or parameterization schemes used [*Smith et al.*, 2011]. *Brunke et al.* [2011] suggested that model errors can affect the estimated fluxes in reanalysis data also. At present, some assessments of the LHF products have already been conducted [e.g., *Zeng et al.*, 2009; *Brunke et al.*, 2011; *Smith et al.*, 2011; *Praveen Kumar et al.*, 2012; *Wang et al.*, 2013] to achieve a better understanding of their performance. Some of them, however, were intercomparisons among LHF products and lacked validation using situ observations [*Brunke et al.*, 2011; *Smith et al.*, 2011]. Even if in situ observations were used, some of the observations might have been assimilated into the reanalysis, thus resulting in a nonindependent evaluation [*Praveen Kumar et al.*, 2012]. In

addition, it is highly possible that an LHF product performs well in a certain region but does not work well in another. Consequently, those products that have been assessed as having good performance in some seas need to be validated by local observations to assess their applicability to regions that have not yet been validated.

The South China Sea (SCS) is the largest marginal sea in the northwestern Pacific, where LHF products are widely used for studying air-sea interaction processes. Since air-sea flux observations in the SCS are relatively scarce, assessments of the LHF products in this area are limited. Based on the sources of such observations, such as research vessels, buoys, and automatic weather stations, *Wang et al.* [2013] evaluated the performances of several LHF products and noted the importance of obtaining high-quality meteorological observations. In recent years, field experiments in the SCS have increased in number [*Yang et al.*, 2015], making it possible to collect more reliable and long-term air-sea flux observations. In this paper, five commonly used LHF products are evaluated against in situ data in order to understand their biases in the SCS. Additionally, the heat budget of the upper ocean in the SCS is of great concern. A large number of studies have shown that the Q_{net} has a prominent effect on the variation in the mixed-layer temperature [e.g., *Wang et al.*, 2002, 2006; *Liu et al.*, 2014; *Tan et al.*, 2016]. A detailed calculation in *Liu et al.* [2014] indicated that the seasonal variation in the Q_{net} was attributed mostly to the seasonal variations in LHF. Therefore, the impacts of the biases in the LHF products on the variations in mixed-layer temperatures in the SCS are explored in this study to provide a reference for optimizing and improving numerical models in the future. Most of the in situ data used in this paper are assuredly not assimilated in any of the reanalysis data sets, which will improve the independence and effectiveness of this evaluation of those reanalysis LHF products.

The rest of this paper is organized as follows: the in situ data and LHF products are introduced in section 2. We evaluate the features of the biases in the LHF products in section 3 and identify their possible causes. In section 4, we estimate the tendency errors of the mixed-layer temperature caused by the biases in the LHF products. Finally, the conclusion and discussion are given in section 5.

2. Data Sets and Methods

2.1. In Situ Data and the Five LHF Products
The available in situ data collected in the SCS for the air-sea fluxes are summarized in Table 1, which contains information such as station name, site coordinates, data type, sampling interval, observational

Table 1. Information About the Observational Stations[a]

Station	Location	Water Depth (m)	Type	Sampling Frequency (min)	Period	Effective Observational Days
Maoming	111.66°E 20.75°N	<100	Buoy	1	*26 May 2010 to 29 Sep 2011*	*413 (MM)*
Shantou	117.34°E 22.33°N	<100	Buoy	1	*16 Oct 2010 to 16 May 2011*	*213 (ST)*
Xisha	112.33°E 16.83°N	~1000	Buoy	10	18 Sep 2009 to 2 Oct 2009	19
					14 Mar 2010 to 4 Apr 2010	22
					24 Apr 2011 to 27 May 2011	34
					24 Aug 2011 to 25 Dec 2011	*124 (XB11)*
					16 May 2012 to 17 Jun 2012	33
					15 Dec 2012 to 7 Apr 2013	*114 (XB13)*
Xisha	112.33°E 16.83°N		Flux tower	10	*26 Apr to 6 Oct 2008*	*164 (XFT)*
Kexue 1	110.26°E 6.41°N	~1300	Mooring buoy	15	7 May 1998 to 20 Jun 1998	33
Shiyan 3	117.40°E 20.60°N	~1000	Mooring buoy	15	6 May 1998 to 23 Jun 1998	38
SCS1	115.60°E 8.10°N	~3000	Buoy	15	19 Apr 1998 to 29 Apr 1998	11
SCS3	114.41°E 12.98°N	~4500	Buoy	15	8 Jun 1998 to 16 Jun 1998	9
SCS3[+]	114.00°E 13.00°N	~4000	Buoy	15	13 Apr 1998 to 29 May 1998	47

[a]The bold italics denote an observational period longer than 100 days. Note that the water depth data are estimated values. The abbreviations in parentheses will be used in the following text.
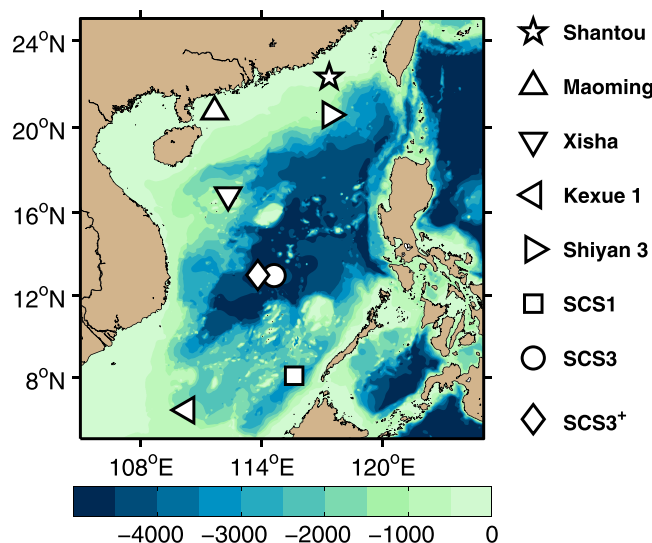
Figure 1. Geographical distribution of all stations in Table 1 and the bathymetric chart of the SCS (units: m).

period, and effective observational days. Figure 1 depicts the geographical distribution of all the stations in Table 1 and the bathymetric chart of the SCS. The stations are located across the northern, central, and southern SCS and cover areas of both shallow and deep waters. The Maoming and Shantou stations provide buoy observations in coastal regions, are approximately 100 km offshore, and have 413 and 213 effective observational days, respectively, from 2010 to 2011. Xisha station provides a series of flux tower observations from April to October 2008 and a series of intermittent buoy observations from September 2009 to April 2013. The flux tower was built on the edge of the reef southwest of Yongxing Island and the buoy was deployed approximately

1.3 km away from the island. In addition, data from five buoy stations from the South China Sea Monsoon Experiment (SCSMEX) are also included in this study. This experiment is of high research value and was used for evaluating LHF products in the SCS by *Wang et al.* [2013].

The five reanalysis data sets that provide the daily LHF and are evaluated in this paper are as follows: the European Centre for Medium Range Weather Forecast (ECWMF) interim reanalysis (ERA-I) [*Dee et al.*, 2011], the National Centers for Environmental Prediction/Department of Energy Global Reanalysis 2 (NCEP2) [*Kanamitsu et al.*, 2002], the Japanese 55 year Reanalysis (JRA55) [*Kobayashi et al.*, 2015], the Objectively Analyzed air-sea Fluxes (OAFlux) [*Yu and Weller*, 2007], and the Flux product in the Tropics (TropFlux) [*Praveen Kumar et al.*, 2012]. Strictly speaking, only the first three are commonly referred to as reanalysis data sets, while the latter two are known as hybrid products [*Smith et al.*, 2011]. For convenience, all of them are classified as reanalysis products in this paper, since the hybrid products use reanalysis data in their production as well. Note that the bulk algorithms are adopted by all these reanalysis products to calculate the LHF. ERA-I is the latest generation of the ECWMF products and has many improvements, such as revised model physics and added background error constraints. NCEP2 is the revised version of the National Centers for Environmental Prediction-the National Center for Atmospheric Research Reanalysis 1 (NCEP/NCAR1) [*Kalnay et al.*, 1996] and has corrections for known errors in satellite measurements. The turbulence and radiation parameterizations in the boundary layer schemes are improved. JRA55 is the second Japanese global atmospheric reanalysis project of the Japan Meteorological Agency (JMA). Compared with the previous product, Japanese 25 year Reanalysis (JRA25) [*Onogi et al.*, 2007], JRA55 uses a new assimilation and prediction system. In particular, a new radiation scheme and variational-bias-correction for satellite observational data are deployed. OAFlux synthesizes the satellite retrievals and reanalysis outputs using a variational objective analysis technique to improve estimates of the air-sea fluxes and provides optimal error estimation. Similar to OAFlux, TropFlux combines multiple sources of data to make an effort to improve the flux estimates in the tropics. This data set only provides data between 30°S and 30°N. ERA-I, JRA55, OAFlux, and TropFlux provide fixed grids with resolutions of 1° × 1°, 1.25° × 1.25°, 1° × 1°, and 1° × 1°, respectively. The NCEP2 has a global T62 Gaussian grid, i.e., a 1.875° interval for longitude and irregular intervals (~1.904°) for latitude.

There are two approaches to building time series of the LHF for representing a certain product. One strategy is to choose the grid point nearest the observational site as a proxy for the product. This approach was used by *Josey* [2001] for their flux evaluation. The other is to find the grid box where a station is covered and then average its four corner points to get the proxy. The results of both methods were compared, and little difference was found. In this study, the first approach was chosen.

2.2. Quality Control and LHF Calculation of the Observational Data

The routine observational variables acquired for the LHF calculation are included for all the stations. Their sampling intervals varied from 1 to 15 min and were subsequently averaged into 30 min interval data. The main steps of the quality control procedure are listed as follows.

1. A preprocess for variable x (x represents U, T_a, T_s, or q_a) is conducted to remove values that are outside a reasonable range. U, T_a, T_s, and q_a are near-surface wind speed, near-surface air temperature, sea surface temperature, and near-surface-specific humidity, respectively. The ranges chosen in this study are 0–60 m s^{-1} for U, 0–40°C for T_a and T_s, and 0–35 g kg^{-1} for q_a. In addition, if the instruments had warning flags, the corresponding records were excluded.
2. The differences between each point adjacent to x are calculated to get a new sequence, Δx, the standard deviation (STD) of which is denoted by $\sigma_{\Delta x}$. Then, every point in Δx is checked to remove the points greater than 5 times of $\sigma_{\Delta x}$. Finally, the removed points are replaced using linear interpolation using the nearest points. No removal will be performed if five continuous points meet the criteria above.
3. A moving average is applied for the bulk variables to obtain the 30 min mean, which is then combined to calculate the LHF according to the bulk algorithm. Since diurnal variation in the LHF is not discussed in this paper, the data are further averaged to produce a daily mean before we evaluate these LHF products.

As *Berry and Kent* [2009] indicated, the bulk algorithm is nonlinear and the random errors of input variables could be transferred to the output flux. Therefore, the 30 min mean fluxes are first obtained instead of using daily variables to calculate the daily fluxes in order to eliminate the effect of random errors as much as possible.

The eddy correlation method is a direct approach to calculating the turbulent flux. However, it is highly dependent on high-frequency observational data and is difficult to conduct for large spatial scales and long periods of time. An indirect approach to the bulk algorithm by *Liu et al.* [1979] is the most widely used one. It is generally expressed as

$$Q_{LH} = \rho L_v C_E U(q_s - q_a),\qquad(1)$$

where ρ is the air density, L_v is the latent heat of evaporation, C_E is the turbulent exchange coefficient for the LHF, U is the wind speed relative to the sea surface (equal to the wind speed at 10 m above the sea surface if the ocean current is not considered), q_s is the sea surface-specific humidity, and q_a is the near-surface-specific humidity. In field observations, q_s and q_a are difficult to observe directly and are usually calculated by

$$q_s = 0.98 \cdot q_{sat}(T_s),\qquad(2)$$

$$q_a = RH \cdot q_{sat}(T_a),\qquad(3)$$

where $q_{sat}(T_s)$ and $q_{sat}(T_a)$ are the saturation-specific humidity at sea surface temperature T_s and the near-surface air temperature T_a (usually 2 m above the sea surface), respectively. An empirical weight coefficient of 0.98 has been proposed extensively to account for the reduction effect of salinity on the saturated vapor pressure [*Fairall et al.*, 1996a,1996b]. RH is the relative humidity, which is a routinely sampled variable in field observations. In equations (1)–(3), U, T_s, T_a, and q_a (derived from RH) are independent variables known as the bulk variables. Various bulk algorithms differ in their parameterization schemes for turbulent exchange coefficients [*Zeng et al.*, 1998; *Brunke et al.*, 2003; *Smith et al.*, 2011]. As evaluated by *Brunke et al.* [2003], the COARE 3.0 algorithm [*Fairall et al.*, 2003] was one of the least problematic and is thus employed in this paper to calculate the turbulent fluxes from in situ observations.

3. Evaluation of the LHF Products

3.1. Comparison Between the LHF Products and Observations

The seasonal climatology of the LHF (1979–2013) in the SCS for the five products is shown in Figure 2, in which positive values mean that the ocean releases heat into the atmosphere. As can be seen in the figure, the SCS loses latent heat in all four seasons, especially the northern SCS in boreal autumn (September–October–November, SON) and winter (December–January–February, DJF). An obvious seasonal cycle can be
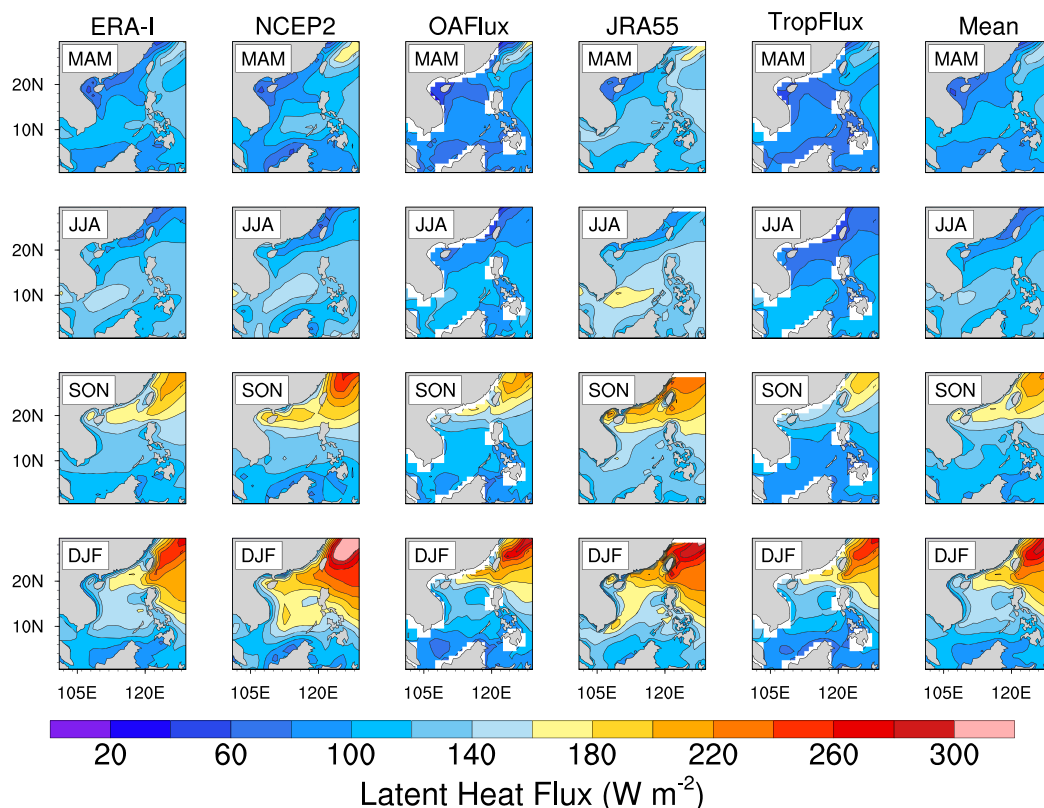
Figure 2. Climatology of the LHF in the SCS. Rows 1–4 represent the boreal spring (MAM), summer (JJA), autumn (SON), and winter (DJF), respectively. Columns 1–5 are ERA-I, NCEP2, OAFlux, JRA55, and TropFlux, and column 6 is the mean of the five products. Note that positive values indicate that the ocean loses heat to the atmosphere.

found in all the LHF products. The basin-mean LHFs in the SCS for DJF and June–July–August (JJA) are 127 and 117 W m^{-2}, respectively. Though the patterns of the five LHF products are similar to each other, there are some notable discrepancies between them. For instance, NCEP2 and JRA55 have much higher LHFs than the data products in SON and DJF. A detailed comparison between the LHF products and observations is given next to show their performances.

Figures 3–5 display the time series of daily LHF of observations and the five products. Except for the stations with too few observational days, such as SCS1 (11 days) and SCS3 (9 days) (Figures 5c and 5d), the LHF products are in good agreement with the observations (Figures 3–5). To comprehensively assess the performances of these LHF products, the total mean biases (see equation (4)), correlation coefficient and root-mean-square error (RMSE) are calculated and shown in Figure 6 using a bar chart and Taylor diagram. To avoid the influences of the short time spans of the observations, only those continuous observations with more than 100 days (missing days not exceeding 10% of the whole period will still be considered continuous) are selected for assessment. Five stations meet this criterion: MM, ST, XFT, XB11, and XB13 (see Table 1).

The total mean bias can indicate whether systematic errors exist in a single LHF product and calculated as

$$Bias = \frac{1}{N}\sum_{i=1}^{N}(PRO_i - OBS_i), \tag{4}$$

where PRO represents the product values, OBS represents the observation values, and $\underline{N}$ is the effective observational days (see in Table 1). In Figure 6a, the performances of ERA-I are different at various stations. ERA-I clearly underestimates the LHF at MM (averaged bias: −19 W m^{-2}) and XB11 (averaged bias: −5 W m^{-2}), and overestimates the LHF at ST (averaged bias: 16 W m^{-2}), XFT (averaged bias: 24 W m^{-2}), and XB13 (averaged bias: 30 W m^{-2}). For OAFlux and TropFlux, they both show no obvious biases (averaged bias: less
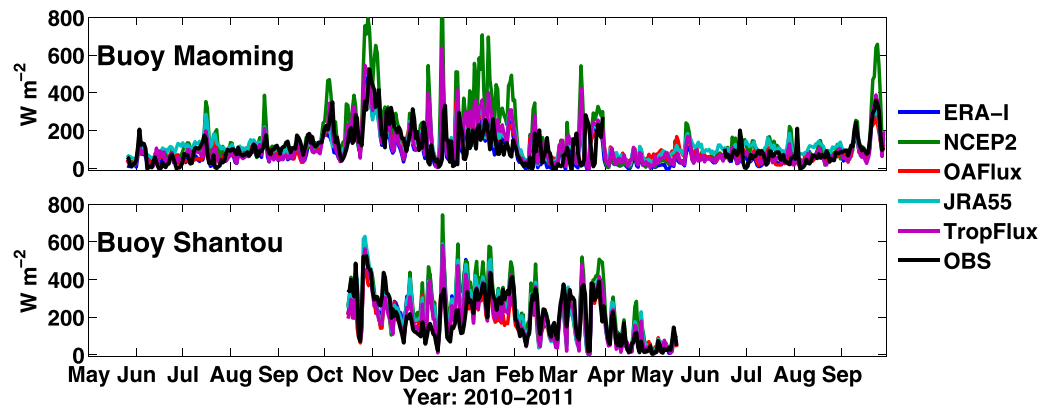
Figure 3. Time series of daily LHF for the five products and observations (black line) at (a) the Maoming station and (b) the Shantou station. The dark blue, green, red, light blue, and purple lines represent ERA-I, NCEP2, OAFlux, JRA55, and TropFlux, respectively.

than 10 W m^{-2}) at most stations except at XB11, where remarkable underestimates of -38 and -39 W m^{-2} are observed, respectively. Except at XB11, NCEP2 (JRA55) overestimates the LHF with biases of 50, 42, 26, and 58 W m^{-2} (20, 22, 43, and 47 W m^{-2}) at MM, ST, XFT, and XB13, respectively. Note that XB11 is the only site where ERA-I, NCEP2, and JRA55 perform well but OAFlux and TropFlux do not. When averaged by weights determined by the number of effective observational days, we find that ERA-I has the smallest mean bias of 2 W m^{-2} as a consequence of its positive (larger than the observation) and negative (smaller than the observation) biases offsetting each other. TropFlux and OAFlux slightly underestimate the LHF
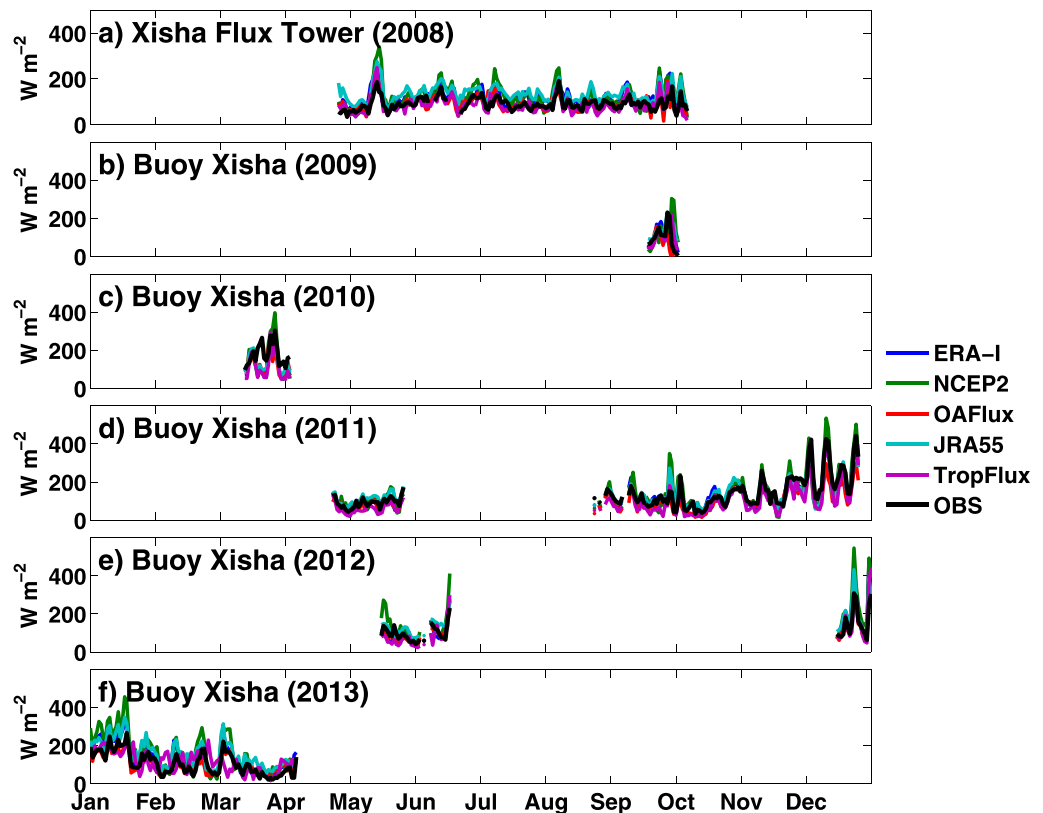

Figure 4. Time series of daily LHF for the five products and observations (black line) at the Xisha station. (a) For the Xisha Flux Tower and (b–f) for the Xisha Buoy from 2009 to 2013, respectively. The dark blue, green, red, light blue, and purple lines represent ERA-I, NCEP2, OAFlux, JRA55, and TropFlux, respectively.
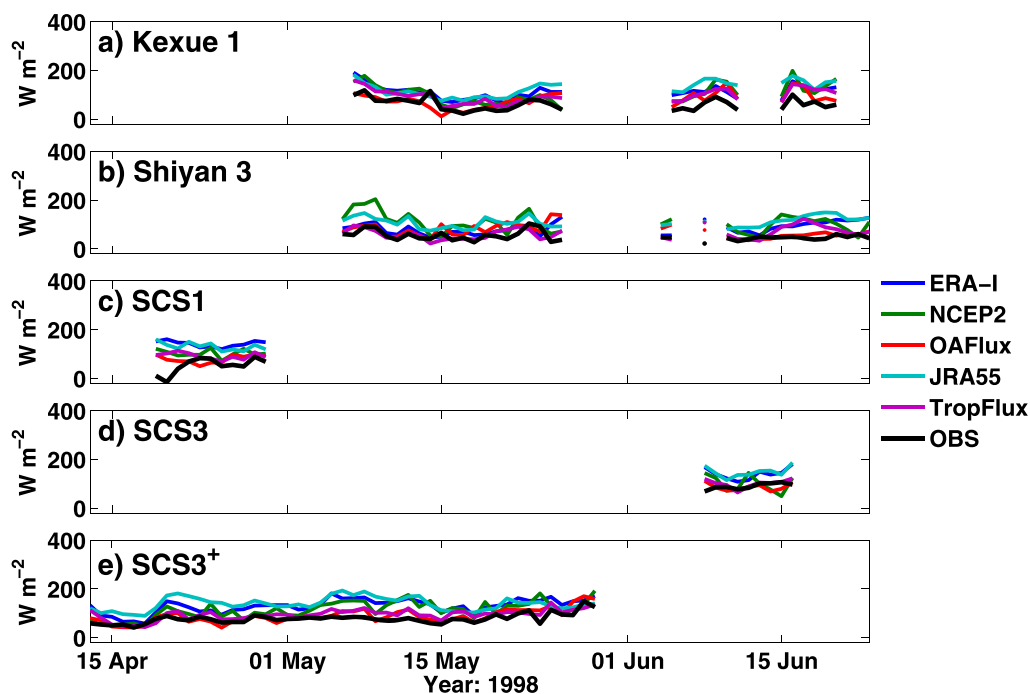
Figure 5. Time series of daily LHF for the five products and observations (black line) at the SCSMEX buoy stations. (a–e) The stations Kexue 1, Shiyan 3, SCS1, SCS3, and SCS3$^+$, respectively. The dark blue, green, red, light blue, and purple lines represent ERA-I, NCEP2, OAFlux, JRA55, and TropFlux, respectively.

with biases of -4 and -6 W m^{-2}, respectively. NCEP2 and JRA55 present serious overestimations of the LHF with biases of 40 and 25 W m^{-2}, respectively.

The Taylor diagram has the ability to display statistics such as the correlation coefficient, amplitude of fluctuation, and RMSE of the data in a single panel [*Taylor*, 2001], which is suitable for comparing the LHF products and observations. It should be noted that the angle of radial lines in the Taylor diagram corresponds to the correlation coefficient, while the length between any point and the origin indicates the amplitude of fluctuation, which is represented by one STD of the data. The amplitude of fluctuation is normalized by the observations so a value of "1" is referred to as "OBS" and the distance from any point to OBS denotes the RMSE with respect to the observations. In Figure 6b, the correlation coefficients between the products and observations are approximately 0.5, 0.8, 0.7, 0.9, and 0.9 at MM, ST, XFT, XB11, and XB13, respectively, and there are no prominent differences between the five products at each site. However, the amplitude of fluctuation for these products behaves much differently. NCEP2 has the largest amplitudes of fluctuation with 1.7, 1.2, 2.0, 1.2, and 1.7 at the five sites mentioned above, respectively. For the other four products, the amplitudes of fluctuation are relatively closer to OBS, ranging from 0.75 to 1.25 except at XFT, where all the amplitudes are larger than OBS. With the data from all sites averaged by weights, OAFlux has the least problematic behavior with an RMSE of 66 W m^{-2}, followed by ERA-I with 71 W m^{-2}, JRA55 with 72 W m^{-2}, and TropFlux with 78 W m^{-2}. The most problematic product is NCEP2 with an RMSE of 102 W m^{-2}.

3.2. Error Analysis
3.2.1. Possible Sources for Biases in the LHF Products
Since LHF is estimated by equation (1), biases in the LHF are likely correlated with the parameterization for the turbulent exchange coefficient and bulk variables [*Brunke et al.*, 2011]. Therefore, possible sources for biases in the LHF products are mainly the exchange coefficient and bulk variables. Here the contributions of the latter are shown below. Due to limited space, the contributions of the former are briefly discussed in section 5.

The scatterplots of the bulk variables from the products and observations are presented in Figure 7 in order to understand the influences on these biases in the LHF products. In general, clear relationships exist within the products and observations. For T_a and T_s, the correlation coefficients between the products and
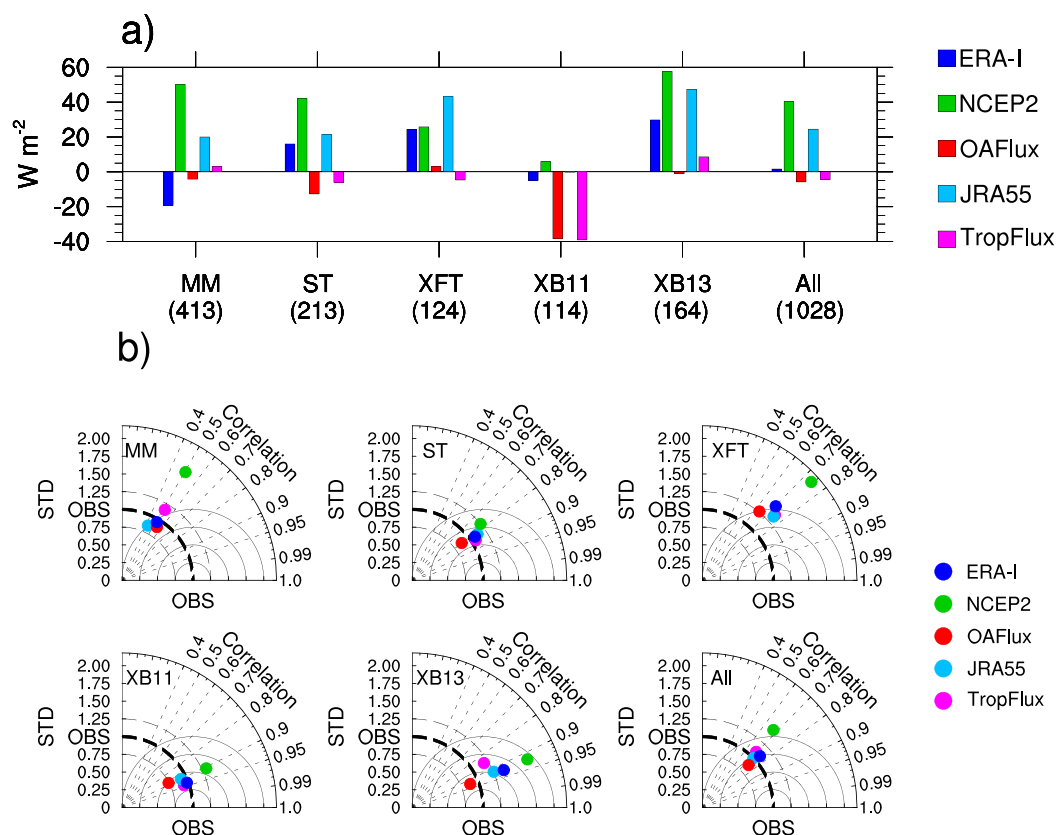
Figure 6. (a) Total mean biases calculated using equations (4) and (b) Taylor diagram of the LHF products. Numbers in parentheses in Figure 6a denote effective observational days. Abbreviations in Figures 6a and 6b are defined in Table 1. "All" in Figures 6a and b denotes the weighted mean results of all stations with respect to effective observational days. The dark blue, green, red, light blue, and purple bars/dots represent ERA-I, NCEP2, OAFlux, JRA55, and TropFlux, respectively. Note that both XB11 and XB13 are at the Xisha station but cover different observational periods of 24 August to 25 December 2011 and 15 December 2012 to 7 April 2013, respectively.

observations reach 0.95 and 0.96 (Figures 7b and 7c), respectively. However, the points are relatively scatted for U and q_a and the correlation coefficients are 0.81 and 0.89 (Figures 7a and 7d), respectively. To understand their relative importance to the biases in the LHF products, the normalized biases of the bulk variables and LHF are compared in Figures 8a–8d. The slopes of the fitting lines are positive for U and T_s, while those for q_a and T_a are negative, and these trends are coincident with the relationship implicated in equations (1–3). Although the correlation coefficients between the biases of the bulk variables and the LHF all exceed the 99% confidence test, some differences are seen. The biases in q_a are mostly correlated with biases in the LHF with a correlation coefficient of −0.68 (Figure 8d), indicating that biases in q_a dominate the biases in the LHF. This result is consistent with the previous results in studies of the north Atlantic [*Bourras et al.*, 2003] and the SCS [*Wang et al.*, 2013]. The effects of the biases in U on the biases in the LHF are slightly weaker than that of q_a with correlation coefficient of 0.54. The T_a and T_s have relatively poor correlations with the biases in the LHF, since the correlation coefficients are −0.36 and 0.19, respectively.

To summarize, the biases in the near-surface-specific humidity and wind speed in the products are the primary sources of the biases in their respective LHFs. In some studies, the cause for biases in the LHF products was attributed to the biases in the difference in the sea-air humidity q_s–q_a [*Chou et al.*, 2004; *Feng and Li*, 2006] which, in fact, does not contradict our results. Our calculation indicates that the biases in q_s–q_a are highly correlated with the biases in q_a.

3.2.2. Seasonal Variation of Biases in the LHF Products and Their Possible Causes

For the in situ data analyzed in this study, the observational periods for the three buoy stations Maoming, Shantou, and Xisha (including XB11 and XB13) are relatively longer in duration and cover both summer and winter (Table 1). Variations of biases in the LHF on the seasonal time scale at these sites are examined.
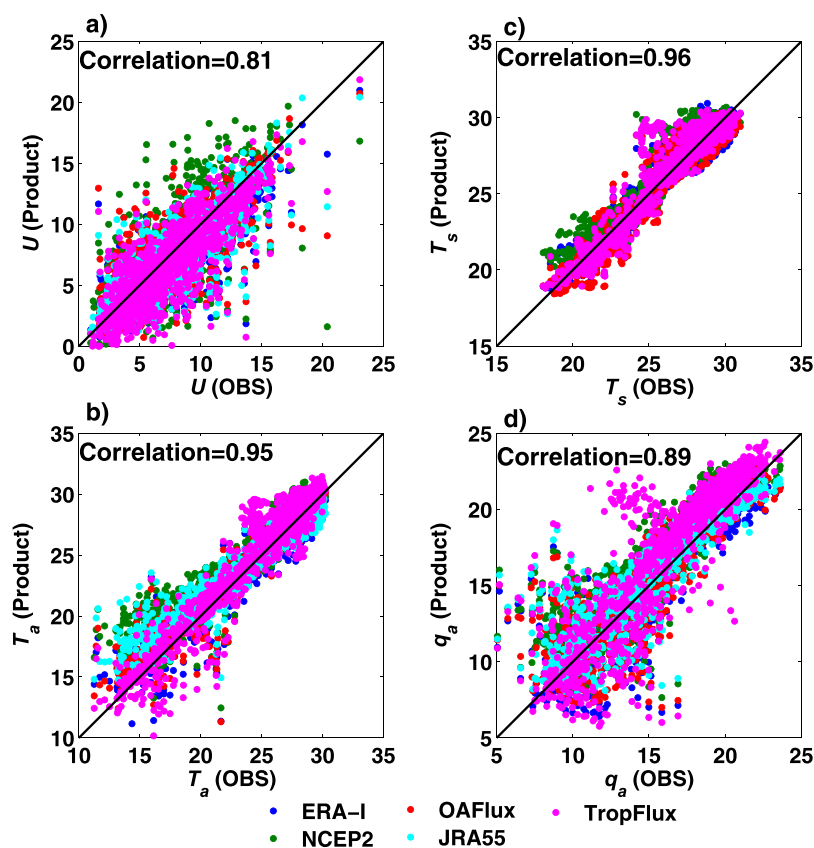
Figure 7. Scatterplots for (a) near-surface wind speed, (b) near-surface air temperature, (c) sea surface temperature, and (d) near-surface-specific humidity with respect to observations. The black line denotes the reference line with a slope of 1. Units of Figures 7a–7d are m s^{-1}, °C, °C, and g kg^{-1}, respectively. The dark blue, green, red, light blue, and purple dots represent ERA-I, NCEP2, OAFlux, JRA55, and TropFlux, respectively. Note that the T_s from JRA55 is not available.

Figures 9a–9c display the monthly LHF at the Maoming, Shantou, and Xisha stations. On a seasonal time scale, the products are generally in agreement with the observations, but biases in magnitude exist. The larger biases in the products appear mostly in winter seasons, such as at the Maoming station in January 2011 (averaged bias: 89 W m^{-2}), the Shantou station in December 2010 (averaged bias: 115 W m^{-2}), and at the Xisha station in December 2011 (averaged bias: −52 W m^{-2}) and January 2013 (averaged bias: 34 W m^{-2}). On the other hand, the smaller biases tend to appear in or around summer seasons, such as at the Maoming station in August 2010 (averaged bias: 5 W m^{-2}) and September 2011 (averaged bias: −4 W m^{-2}), at the Shantou station in May 2011 (averaged bias: 0 W m^{-2}), and at the Xisha station in June 2012 (averaged bias: 4 W m^{-2}). Figures 9d–9f indicate that the biases in the LHF products have remarkable seasonal variations. In total, the mean biases in the products are 37 W m^{-2} in winter (DJF) and 12 W m^{-2} in summer (JJA) with a difference of 25 W m^{-2}.

As mentioned above, the main sources of the biases in the LHF products come from the biases in the near-surface-specific humidity and wind speed in the reanalysis. Further analysis shows that the seasonal varia-tion in the biases also has a distinct relationship, which is depicted by the monthly mean biases of q_a and U in Figures 9d–9f. For q_a, its positive (negative) biases are highly correlated with the negative (positive) biases in the LHF products. For instance, the biases of q_a at the Maoming station in January 2011, at the Shantou station in December 2010, and at the Xisha station in January 2013 were −1.5, −2.2, and −2.3 g kg^{-1}, respectively, consistent with the times when the biases in the LHF reached their peaks (Figure 9d). For U, its positive (negative) biases are correlated with the positive (negative) biases in the LHF products. For instance, the negative biases in U gradually increased at the Xisha station from September to December 2011 as did the negative biases in the LHF products. When the biases in U reached their peaks at the Xisha station in December 2011 and January 2013, the biases in the LHF products peaked as well. Although biases
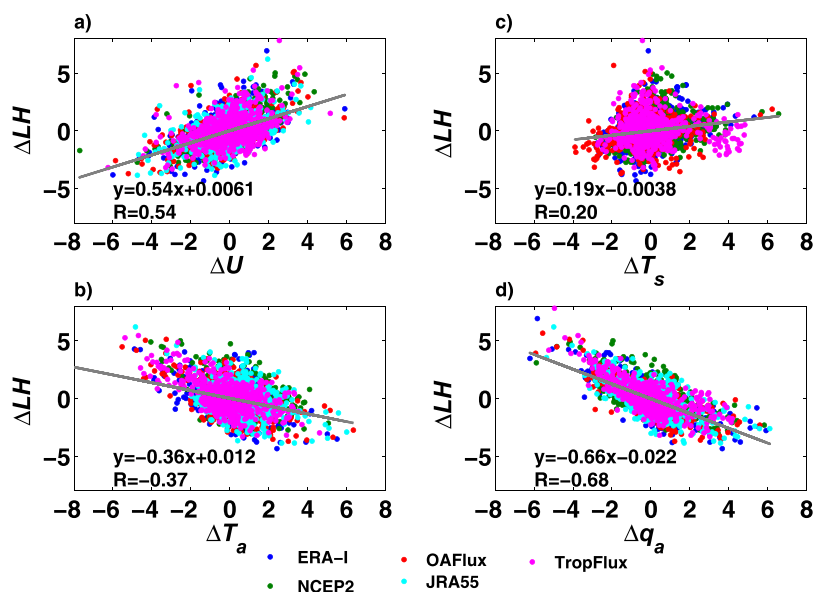
Figure 8. Scatterplots for the biases of (a) near-surface wind speed, (b) near-surface air temperature, (c) sea surface temperature, and (d) near-surface-specific humidity with respect to the biases of LHF. The gray line denotes the least square fit. The expression for the gray line and correlation "R" are given in the lower left corner of each plot. All the data are normalized first. The dark blue, green, red, light blue, and purple dots represent ERA-I, NCEP2, OAFlux, JRA55, and TropFlux, respectively. Note that the T_s from JRA55 is not available.

in both q_a and U can influence the biases in the LHF products, their impacts are different. For instance, the variances of the biases in U were not quite obvious at the Maoming and Shantou stations in each season. Specifically, when the biases in U were close to zero at the Maoming station in November 2010 and January
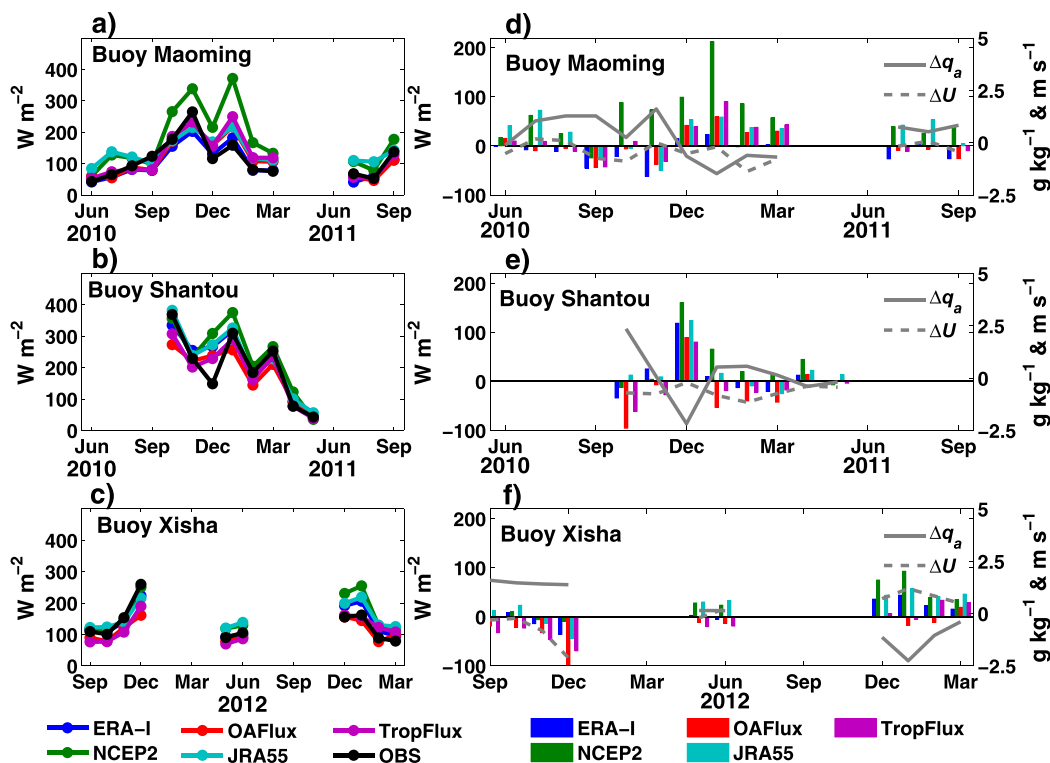

Figure 9. (a–c) Monthly LHF values of the five products and observations (black line) and (d–f) biases in the LHF of the five products. (top) For the Maoming, (middle) Shantou, and (bottom) Xisha buoy stations. The solid and dashed gray lines in Figures 9d–9f denote the monthly biases of near-surface-specific humidity and wind speed, respectively. The dark blue, green, red, light blue, and purple lines/bars represent ERA-I, NCEP2, OAFlux, JRA55, and TropFlux, respectively.
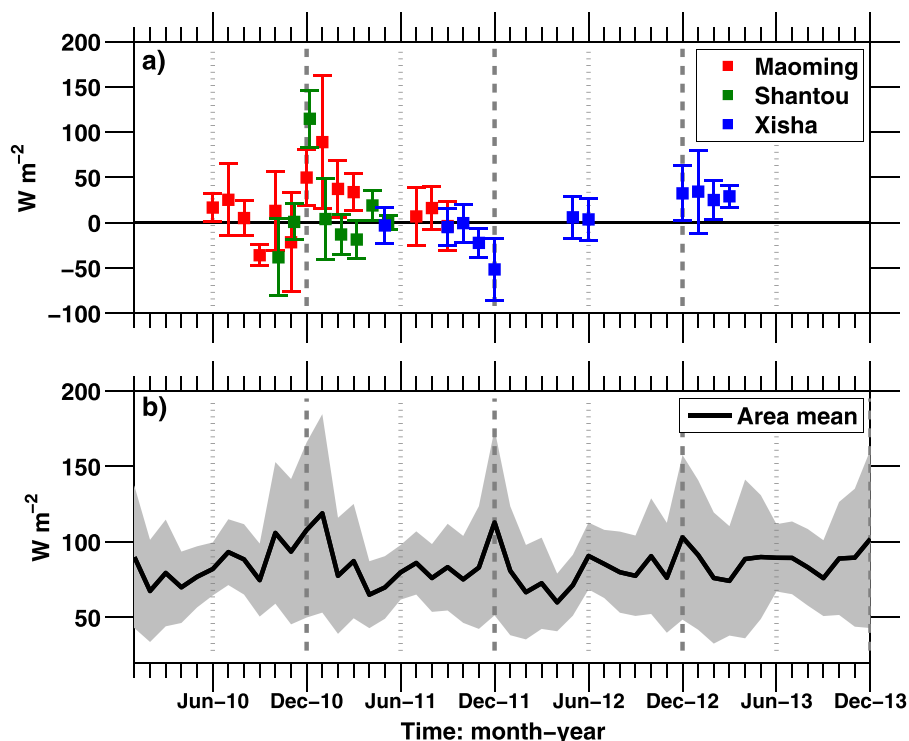
Figure 10. (a) Monthly biases of LHF products at Maoming (red squares), Shantou (green squares), and Xisha (blue squares) stations; and (b) area-mean LHF in the SCS (black line). The squares in Figure 10a and black line in Figure 10b denote the mean values of the five products. The error bars in Figure 10a and filled area in Figure 10b are equal to the STD of the five products. The dotted and dashed gray vertical lines indicate June and December, respectively.

2011, and at the Shantou station in December 2010, the biases in the LHF products peaked during those months. On the other hand, at the Xisha station, the biases of U and LHF varied more consistently, while the biases in q_a remained nearly unchanged over time. Therefore, both the biases in q_a and U are the key factors that influence the seasonal variations in the biases in the LHF products.

Seasonal variation is found not only in the biases of the LHF products with respect to the observations but also in the differences among the five LHF products. To reveal the seasonal variations in the differences among the five LHF products, their mean values and STD are calculated for each month (Figure 10). As shown in Figure 10a, the larger error bars appear around December while the smaller ones are around June of each year, indicating that the differences among the LHF products are more obvious in winter than in summer. For instance, the STDs are 44 W m^{-2} at the Shantou station in January 2011, 73 W m^{-2} at the Maoming station in January 2011, and 45 W m^{-2} at the Xisha station in January 2013. On the other hand, they decreased to 8 W m^{-2} at the Shantou station in May 2011, 15 W m^{-2} at the Maoming station in June 2010, and 23 W m^{-2} at the Xisha station in June 2012. It is noteworthy that the observations are discontinuous in time and the number of observational sites is quite limited. To further identify the features of the differences among the LHF products, the area-mean LHF in the SCS (108°E–120°E, 6°N–24°N) of the five products is calculated. In Figure 10b, the black curve denotes the monthly mean LHF of the five products from 2010 to 2013, and the gray area is the STD for the variance of the five products. It is shown that differences among the LHF products often reach their peak around December and decrease to the smallest values around June every year. The averaged STD values for DJF and JJA are 55 and 19 W m^{-2}, respectively, which means that significant seasonal variation exists in the differences among the LHF products.

4. Impacts of the Biases in the LHF Products on the Mixed-Layer Temperature

The air-sea fluxes are usually used to drive ocean models and coupled ocean-atmosphere models [i.e., *Chou et al.*, 2004; *Delworth et al.*, 2016]. Their substantial impacts on these models are reflected in terms of the momentum equation (momentum flux) and thermal equation (heat fluxes) [*Chaudhuri et al.*, 2013].

Therefore, the biases in the heat fluxes may cause uncertainty in simulations of the heat budget in the ocean models. Previous studies have shown that Q_{net} had prominent effects on the variation in the mixed-layer temperature in the SCS [*Wang et al.*, 2002, 2006; *Liu et al.*, 2014; *Tan et al.*, 2016]. This study aims to explore to what extent these biases in the LHF would induce changes in the simulated mixed-layer temperature in the SCS.

If only the heat flux term is concerned, the heat budget of the mixed-layer temperature can be simplified as

$$\frac{dT_{MLD}}{dt} \approx \frac{Q_{net}}{\rho c_p h_{MLD}}, \tag{5}$$

where the leftmost term denotes the variation tendency of the mixed-layer temperature over a period of time (one month used in this paper), ρ is the density of seawater, c_p is the heat capacity of sea water, and h_{MLD} is the mixed-layer depth. The SWR flux, LWR flux, LHF, and SHF are the four components of Q_{net}. To illustrate the influences of the biases of the LHF on the mixed-layer temperature, equation (5) is rewritten as

$$\frac{dT_{MLD}}{dt} \approx \frac{LHF_{err}}{\rho c_p h_{MLD}}, \tag{6}$$

where LHF_{err} represents the biases in the LHF. It is further estimated by the averaged biases in the LHF for months n and $n-1$; that is,

$$\overline{LHF_{err}}^n = \frac{1}{2}\left(\overline{LHF_{err}}^n + \overline{LHF_{err}}^{n-1}\right). \tag{7}$$

From equations (6) to (7), the uncertainty in the variation tendency of the mixed-layer temperature is determined by the biases in the LHF and the mixed-layer depth together. Since there were no direct observations of the mixed-layer depth around the stations, data for about the mixed-layer depth from Levitus [*Levitus and Boyer*, 1994] were considered as substitutes in this study. The Levitus climatological data were objectively analyzed fields of major ocean parameters, which were derived from a set of observational profiles with critical quality controls. For heat budget analyses of upper ocean in the SCS, the mixed-layer depth in the Levitus climatology is usually used [e.g., *Wang et al.*, 2006; *Tan et al.*, 2016]. For the purposes of making our results more comparable and relatable to those of others, the Levitus climatology data were used in this paper. The climatology data for the mixed-layer depth at the Maoming, Shantou, and Xisha stations are displayed in Figure 11, where remarkable seasonal cycles can be seen. For these three stations, the thickest mixed layers all occurred in January at 24.5, 43.9, and 39.9 m, respectively, while the thinnest ones were all in June at 3.0, 4.2, and 12.1 m, respectively. Though both are located in coastal regions, the thickness of mixed layer at the Shantou station is larger than that at the Maoming station except for April. In addition, the annual amplitude at the Shantou station is around 2 times as large as that at the Maoming station. For the months of January–March and October–December, the thickness of the mixed layer at the Shantou station is even larger than that at the Xisha station in the deep sea. The clear variation occurred at the Shantou station may be associated with the fact that it is located in the northeastern SCS, which is on the path of Kuroshio intrusion and influenced by the strong western boundary current [*Yu et al.*, 2006].
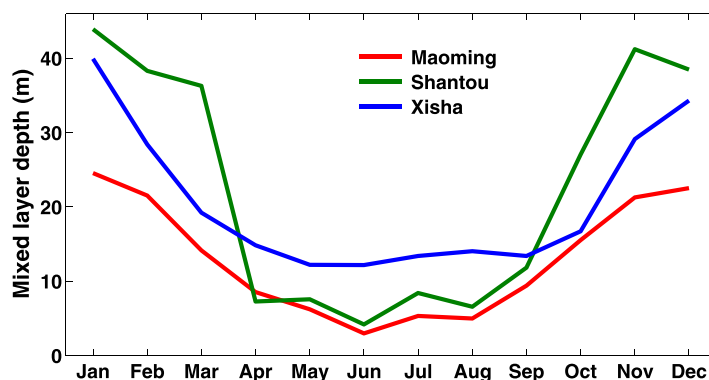

Figure 11. Climatology for the mixed-layer depth at Maoming (red line), Shantou (green line), and Xisha (blue line) stations. The data are from Levitus (http://iridl.ldeo.columbia.edu/SOURCES/.LEVITUS/).

The estimated uncertainty for the variation tendency of the mixed-layer temperature is shown in Figure 12. As mentioned above, biases in the LHF products are larger in the winter than in summer. However, the largest positive error in the mixed-layer temperature tendency was at the Maoming station in the summer season (July 2010 for 3.5°C/month), and the largest negative
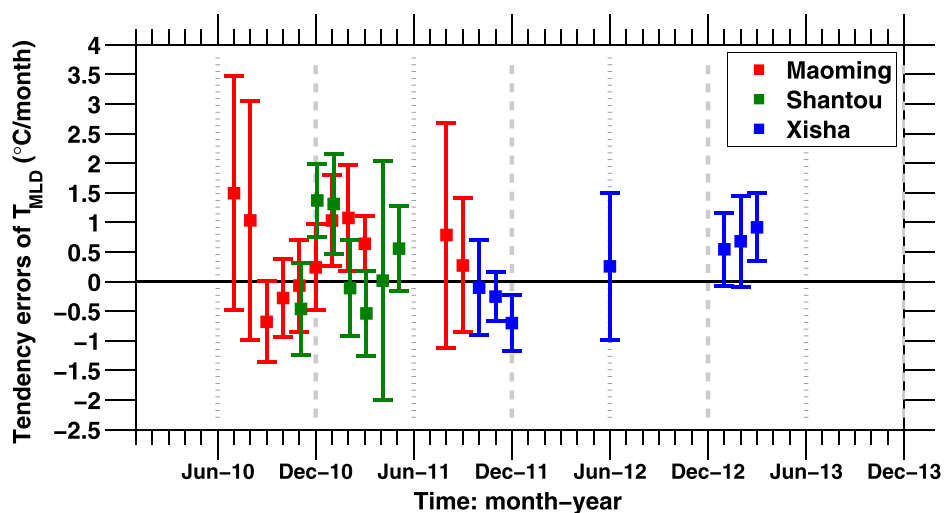
Figure 12. The tendency of the mixed-layer temperature estimated by biases in the LHF products at stations Maoming (red squares), Shantou (green squares), and Xisha (blue squares). The squares denote the mean values of the five products. The error bars are equal to the STD of the five products. The dotted and dashed gray lines indicate June and December, respectively.

one was at the Shantou station in summer season (April 2011 for −2°C/month), a dynamic that is associated with the thicker mixed layer in winter than in summer. As in equation (6), considering that the mixed-layer depth is in the position of the denominator, even smaller (larger) biases in the LHF in summer (winter) can be amplified (reduced) by a thinner (thicker) mixed layer. Consequently, the errors caused by biases in the LHF are even greater in summer than in winter. The long error bars also indicate that significant differences exist in those LHF products, which can be as high as 2°C/month (in July and August 2010, and in August 2011 at the Maoming station). It is noteworthy that the errors for the variation tendency of the mixed-layer temperature can be reduced to −0.7 to 1.5°C/month if all five products are first averaged.

5. Summary and Discussion

5.1. Summary

A number of studies have shown that the LHF is closely related to different phenomena in the air-sea coupled systems on various time scales. On scales from synoptic to seasonal, for example, the LHF plays important roles in the formation, development, and maintenance of storm tracks [*Cayan*, 1992], tropical cyclones [*Chen et al.*, 2013; *Shi et al.*, 2015], intraseasonal oscillations [*Sobel et al.*, 2008; *Gao et al.*, 2016], and others. At larger scales, variations in the LHF exchange are key mechanisms for explaining the wind-evaporation-SST feedbacks involved in events such as the Indian Ocean Dipole [*Praveen Kumar et al.*, 2012] and the El Niño-Southern Oscillation [*Chatterjee et al.*, 2016]. Errors in estimating the LHF will have an effect on our studies of the phenomena mentioned above. Therefore, obtaining more accurate LHF data is one of the prerequisites for diagnosing air-sea interactions.

Using in situ data collected on the air-sea flux in the SCS, we evaluated five commonly used LHF products (ERA-I, NCEP2, OAFlux, JRA55, and TropFlux). The analyses suggest that the LHF products coincide well with the observations in terms of temporal variation. However, comparing observations reveals that biases do exist in the LHF products. In terms of the mean biases, ERA-I has the smallest mean bias (2 W m^{-2}). TropFlux (−4 W m^{-2}), and OAFlux (−6 W m^{-2}) slightly underestimate the LHF. JRA55 (25 W m^{-2}) and NCEP2 (40 W m^{-2}) overestimate the LHF greatly. Regarding the RMSEs, OAFlux has the smallest RMSEs (66 W m^{-2}), followed by ERA-I (71 W m^{-2}), JRA55 (72 W m^{-2}), TropFlux (78 W m^{-2}), and NCEP2 (102 W m^{-2}). In general, for studies referring to the five LHF products evaluated in this study, we conclude that OAFlux and ERA-I are better choices for the SCS. As assessments of these LHF products are limited for the SCS, to objectively evaluate them requires more and longer observations in more regions. It is worth noting that, even if a product is less problematic on the whole, it could have poor performances for some regions and/or some periods. For instance, OAFlux and TropFlux are consistent with the observations except at XB11, where clear underestimates can be found.

The biases in the LHF products show prominent seasonal variation, which is higher in winter than in summer. Therefore, when using the LHF products, special attention should be paid to their performances in winter. In addition, differences among the LHF products are nonnegligible and exhibit features of seasonal variation, which tend to peak in winter. Considering the diversity of the various LHF products, it is important to choose the proper LHF product for one's study.

With the simplified thermal equation, it is found that the tendency errors of the mixed-layer temperature caused by biases in the LHF products are significant in both winter and summer in the SCS. Specifically, the errors in summer are more obvious because a thinner mixed layer in summer can amplify the effect of even a small bias in the LHF products. In general, the tendency errors vary in the range of -2.0 to $3.5°$C/month. With all the products averaged first, the errors can be reduced to -0.7 to $1.5°$C/month, indicating that ensemble means of the five LHF products could substantially reduce the uncertainties of the estimated mixed-layer temperature tendency in the SCS. This provides a more reasonable application of the LHF products, i.e., using the mean field from various products to effectively reduce potential errors that exist in any single product.

According to the bulk formula, the possible sources for the biases in the LHF products are focused in the bulk variables. The formula shows that biases in the near-surface-specific humidity are the most notable causes for biases in the LHF, followed by those in the near-surface wind speed. Compared with the near-surface humidity and wind speed, the impacts of the biases in the near-surface air temperature and sea surface temperature are not clear. To improve the accuracies of LHF data, estimations of near-surface-specific humidity data should be enhanced first for those products.

5.2. Discussion

In addition to the bulk variables, uncertainties in the turbulent exchange coefficient are also important for explaining biases in the LHF products. The parameterization for the turbulent exchange coefficient can be affected by factors such as atmospheric stratification, gust effect, wave state, and others. The parameterization of exchange coefficients in high wind has been a hot topic in recent years. Both laboratory results [*Haus et al.*, 2010] and field observations [*Zhang et al.*, 2008] have indicated that the variations in the exchange coefficients in high wind were quite different from those in moderate wind. Some of our observed wind speeds reached the high wind level; however, for parametric studies, high-frequency observations from several Hz to tens of Hz are essential based on the eddy covariance (EC) method. In this study, no EC systems were installed at the sites and all of the surface data were measured by gradient instruments with much slower frequencies. Consequently, the exchange coefficients could not be obtained from the in situ data and the observational LHF was calculated using the bulk method from COARE 3.0. Our limited knowledge of the parameterization of the exchange coefficients would probably, to some degree, lead to uncertainties in the estimates of LHF under high wind conditions. This is a problem that could be resolved with more observational data under extreme conditions in the future. It is also an important way to develop more reliable and applicable parameterization schemes for exchange coefficients to improve the performances of the LHF products.

Recently, some studies had focused on the effect of water depth on the drag coefficient C_D [*Toffoli et al.*, 2012]. Although their studies mainly focused on C_D, the latent heat exchange coefficient C_E can be inferred to be influenced by water depth as well, taking into account the close relationship between C_E and C_D. As can be expressed as a function of C_D, the variations of C_E are highly correlated with C_D. For example, a linear relationship between C_E and the square root of C_D was suggested by *DeCosmo et al.* [1996] under neutral conditions. Their close relationships are also reflected in the regular variations of the C_K/C_D ratio, where C_K is the exchange coefficient of enthalpy flux and is usually assumed to be equal to C_E [*Zhang et al.*, 2008]. In a word, it is assumed that water depth can impact C_E as well as C_D. As observational stations from both coastal regions and deep sea are included in this study, the possible impact of water depth on the performance of LHF products is discussed below.

In Figure 6b, the data for XFT were acquired by a flux tower, and no comparison could be performed with other data of the same type; as such, these data are excluded in the following analysis. At the other four sites, it is notable that the correlations between the LHF products and observations are lower at MM ($\sim$0.5) and ST ($\sim$0.8) than at XB11 ($\sim$0.9) and XB13 ($\sim$0.9). One remarkable difference among these sites is that MM and ST are located in coastal regions with water depths less than 100 m, while XB11 and XB13 are at
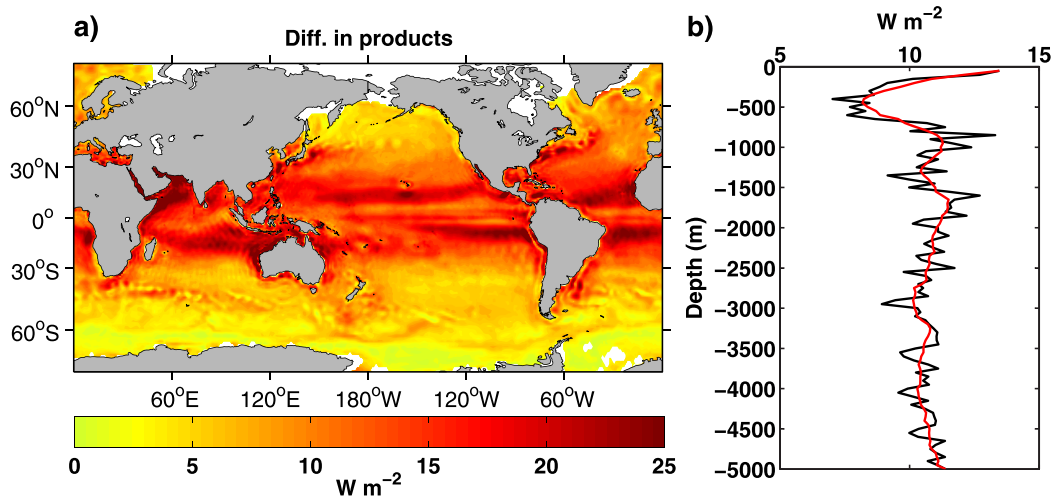
Figure 13. (a) Spatial distribution of the differences in the climatology of the ERA-I, NCEP2, OAFlux, and JRA55 and (b) their variation with depth. The difference is defined as the square root of the variance of the four LHF products at each grid. The black curve in Figure 13b is the initial result at every 50 m interval, and the red is the nine-point-running mean. The four LHF products are interpolated at a resolution of $1° \times 1°$, and the climatology refers to the period from 1979 to 2013.

deep sea locations with water depths $\sim$1000 m, it is assumed that the performance of LHF products may be affected by water depth to some degree. In coastal regions, the uncertainty of the parameterization for turbulent exchange coefficient, if it exists, would possibly result in biases in the LHF products to some degree. Furthermore, if distinct biases exist in the LHF for those products, there would be conspicuous differences between them. To verify this assumption, the differences between ERA-I, NCEP2, OAFlux, and JRA55 (Trop-Flux is not included since it only covers tropical areas) are calculated, defined as the square root of the variance for the four products at each grid point. The results show that the globally averaged difference between the four products is approximately 11 W m^{-2}, with much higher values in the tropical and subtropical regions than in mid and high latitudes (Figure 13a). Additionally, in the tropical and subtropical regions, differences around coastal regions are quite obvious, e.g., in the coasts of northern Arabian Sea, east and south of China, north and west of Austria, and east of America. The variations in the differences in the LHF products with respect to water depth are further illustrated in Figure 13b. It is found that (1) in depths of 0–500 m, the differences are approximately 5 W m^{-2}, which becomes more evident at shallower depths; (2) in the range of 500–1000 m, the differences increase with depth; and (3) in the range of 1000 m and deeper, no remarkable changes are observed and the differences seem to be stable at approximately 11 W m^{-2}. In summary, the four LHF products do have significant discrepancies in coastal regions, which is possibly a consequence of the turbulent exchange coefficient being influenced by water depth, which is currently not reflected in the parameterization. This may cause the products perform less well in coastal regions. Improvements in the parameterization of variables in coastal regions are needed in future studies. There is another interesting issue between the two coastal stations of Maoming and Shantou: the products perform less well at the Maoming station than at the Shantou station (Figure 6b). One significant difference between the two sites is in their variations in mixed-layer depth (Figure 11). The Shantou station has a thicker mixed layer with an annual amplitude about 2 times of that at the Maoming station. This feature of the mixed layer may be another potential factor affecting the performances of the LHF products. A thinner, weaker fluctuating mixed layer tends to cause a poorer performance of LHF products, which remains to be further explored in the next step.

References

Berry, D. I., and E. C. Kent (2009), A new air–sea interaction gridded dataset from ICOADS with uncertainty estimates, *Bull. Am. Meteorol. Soc.*, *90*, 645–656, doi:10.1175/2008BAMS2639.1.

Bourras, D. (2006), Comparison of five satellite-derived latent heat flux products to moored buoy data, *J. Clim.*, *19*, 6291–6313, doi:10.1175/JCLI3977.1.

Bourras, D., W. T. Liu, L. Eymard, and W. Tang (2003), Evaluation of latent heat flux fields from satellites and models during SEMAPHORE, *J. Appl. Meteorol.*, *42*, 227–239, doi:10.1175/1520-0450(2003)042<0227:EOLHFF>2.0.CO;2.

Brunke, M. A., C. W. Fairall, X. Zeng, L. Eymard, and J. A. Curry (2003), Which bulk aerodynamic algorithms are least problematic in computing ocean surface turbulent fluxes?, *J. Clim.*, *16*, 619–635, doi:10.1175/1520-0442(2003)016<0619:WBAAAL>2.0.CO;2.

Brunke, M. A., Z. Wang, X. Zeng, M. Bosilovich, and C.-L. Shie (2011), An assessment of the uncertainties in ocean surface turbulent fluxes in 11 reanalysis, satellite-derived, and combined global datasets, *J. Clim.*, *24*, 5469–5493, doi:10.1175/2011JCLI4223.1.

Cayan, D. R. (1992), Latent and sensible heat flux anomalies over the northern oceans: The connection to monthly atmospheric circulation, *J. Clim.*, *5*, 354–370.

Chatterjee, S., M. Nuncio, and K. Satheesan (2016), ENSO related SST anomalies and relation with surface heat fluxes over south Pacific and Atlantic, *Clim. Dyn.*, 1–11, doi:10.1007/s00382-016-3349-3.

Chaudhuri, A. H., R. M. Ponte, G. Forget, and P. Heimbach (2013), A comparison of atmospheric reanalysis surface products over the ocean and implications for uncertainties in air-sea boundary forcing, *J. Clim.*, *26*, 153–170, doi:10.1175/JCLI-D-12-00090.1.

Chen, S., W. Li, Y. Lu, and Z. Wen (2013), Variations of latent heat flux during tropical cyclones over the South China Sea, *Meteorol. Appl.*, *21*, 717–723.

Chou, S.-H., E. Nelkin, J. Ardizzone, R. M. Atlas, and C.-L. Shie (2003), Surface turbulent heat and momentum fluxes over global oceans based on the Goddard satellite retrievals, version 2 (GSSTF2), *J. Clim.*, *16*, 3256–3273, doi:10.1175/1520-0442(2003)016<3256:STHAMF>2.0.CO;2.

Chou, S.-H., E. Nelkin, J. Ardizzone, and R. M. Atlas (2004), A comparison of latent heat fluxes over global oceans for four flux products, *J. Clim.*, *17*, 3973–3989, doi:10.1175/1520-0442(2004)017<3973:ACOLHF>2.0.CO;2.

DeCosmo, J., K. B. Katsaros, S. D. Smith, R. J. Anderson, W. A. Oost, K. Bumke, and H. Chadwick (1996), Air-sea exchange of water vapor and sensible heat: The humidity exchange over the sea (HEXOS) results, *J. Geophys. Res.*, *101*(C5), 12,001–12,016.

Dee, D. P., et al. (2011), The ERA-Interim reanalysis: Configuration and performance of the data assimilation system, *Q. J. R. Meteorol. Soc.*, *137*, 553–597, doi:10.1002/qj.828.

Delworth, T. L., F. Zeng, G. A. Vecchi, X. Yang, L. Zhang, and R. Zhang (2016), The North Atlantic Oscillation as a driver of rapid climate change in the Northern Hemisphere, *Nat. Geosci.*, *9*(7), 509–512.

Fairall, C. W., E. F. Bradley, J. S. Godfrey, G. A. Wick, J. B. Edson, and G. S. Young (1996a), Cool-skin and warm-layer effects on sea surface temperature, *J. Geophys. Res.*, *101*(C1), 1295–1308, doi:10.1029/95JC03190.

Fairall, C. W., E. F. Bradley, D. P. Rogers, J. B. Edson, and G. S. Young (1996b), Bulk parameterization of air-sea fluxes for Tropical Ocean-Global Atmosphere Coupled–Ocean Atmosphere Response Experiment, *J. Geophys. Res.*, *101*(C2), 3747–3764.

Fairall, C. W., E. F. Bradley, J. E. Hare, A. A. Grachev, and J. B. Edson (2003), Bulk parameterization of air-sea fluxes: Updates and verification for the COARE algorithm, *J. Clim.*, *16*, 571–591, doi:10.1175/1520-0442(2003)016<0571:BPOASF>2.0.CO;2.

Feng, C., and J. Li (2006), A comparison of latent heat fluxes over global oceans for ERA and NCEP with GSSTF2, *Geophys. Res. Lett.*, *33*, L03810, doi:10.1029/2005GL024677.

Gao, Y., P. C. Hsu, and H. H. Hsu (2016), Assessment of surface latent heat flux associated with the Madden-Julian Oscillation in reanalysis, *Clim. Dyn.*, *47*, 1755–1774, doi:10.1007/s00382-015-2931-4.

Grodsky, S. A., A. Bentamy, J. A. Carton, and R. T. Pinker (2009), Intraseasonal latent heat flux based on satellite observations, *J. Clim.*, *22*, 4539–4556, doi:10.1175/2009JCLI2901.1.

Haus, B. K., D. Jeong, M. A. Donelan, J. A. Zhang, and I. Savelyev (2010), Relative rates of sea air heat transfer and frictional drag in very high winds, *Geophys. Res. Lett.*, *37*, L07802, doi:10.1029/2009GL042206.

Josey, S. A. (2001), A comparison of ECMWF, NCEP–NCAR, and SOC surface heat fluxes with moored buoy measurements in the subduction region of the Northeast Atlantic, *J. Clim.*, *14*, 1780–1789, doi:10.1175/1520-0442(2001)014<1780:ACOENN>2.0.CO;2.

Kalnay, E., et al. (1996), The NCEP/NCAR 40-year reanalysis project, *Bull. Am. Meteorol. Soc.*, *77*, 437–471, doi:10.1175/1520-0477(1996)077<0437:TNYRP>2.0.CO;2.

Kanamitsu, M., W. Ebisuzaki, J. Woollen, S.-K. Yang, J. J. Hnilo, M. Fiorino, and G. L. Potter (2002), NCEP-DOE AMIP-II reanalysis (R–2), *Bull. Am. Meteorol. Soc.*, *83*, 1631–1643, doi:10.1175/BAMS-83-11-1631.

Kobayashi, S., et al. (2015), The JRA-55 reanalysis: General specifications and basic characteristics, *J. Meteorol. Soc. Jpn.*, *93*(1), 5–48, doi:10.2151/jmsj.2015-001.

Kubota, M., A. Kano, H. Muramatsu, and H. Tomita (2003), Intercomparison of various surface latent heat flux fields, *J. Clim.*, *16*, 670–678, doi:10.1175/1520-0442(2003)016<0670:IOVSLH>2.0.CO;2.

Levitus, S., and T. P. Boyer (1994), *World Ocean Atlas 1994, Temperature*, NOAA Atlas NESDIS, vol. 4, NOAA, Silver Spring, Md.

Liu, J., J. A. Curry, C. A. Clayson, and M. A. Bourassa (2011), High-resolution satellite surface latent heat fluxes in North Atlantic hurricanes, *Mon. Weather Rev.*, *139*, 2735–2747, doi:10.1175/2011MWR3548.1.

Liu, Q.-Y., D. Wang, X. Wang, Y. Shu, Q. Xie, and J. Chen (2014), Thermal variations in the South China Sea associated with the eastern and central Pacific El Niño events and their mechanisms, *J. Geophys. Res. Oceans*, *119*, 8955–8972, doi:10.1002/2014JC010429.

Liu, W. T., K. B. Katsaros, and J. A. Businger (1979), Bulk parameterization of air–sea exchanges of heat and water vapor including the molecular constraints at the interface, *J. Atmos. Sci.*, *36*, 1722–1735, doi:10.1175/1520-0469(1979)036<1722:BPOASE>2.0.CO;2.

Onogi, K., et al. (2007), The JRA-25 reanalysis, *J. Meteorol. Soc. Jpn.*, *85*, 369–432.

Praveen Kumar, B., J. Vialard, M. Lengaigne, V. S. N. Murty, and M. J. McPhaden (2012), TropFlux: Air-sea fluxes for the global tropical oceans–description and evaluation, *Clim. Dyn.*, *38*, 1521–1543, doi:10.1007/s00382-011-1115-0.

Schulz J., J. Meywerk, S. Ewald, and P. Schlüssel (1997), Evaluation of satellite-derived latent heat fluxes, *J. Clim.*, *10*, 2782–2795, doi:10.1175/1520-0442(1997)010<2782:EOSDLH>2.0.CO;2.

Shi, R., L. Zeng, J. Chen, L. Yang, L. Dong, Y. He, D. Li, and J. Yao (2015), Observation and numerical simulation of the marine meteorology elements and air-sea fluxes at Yongxing Island in September 2013, *Aquat. Ecosyst. Health Manage.*, *18*, 394–402.

Singh, R., P. C. Joshi, and C. M. Kishtawal (2005), A new technique for estimation of surface latent heat fluxes using satellite-based observations, *Mon. Weather Rev.*, *133*, 2692–2710, doi:10.1175/MWR2993.1.

Smith, S. R., P. J. Hughes, and M. A. Bourassa (2011), A comparison of nine monthly air-sea flux products, *Int. J. Clim.*, *31*, 1002–1027, doi:10.1002/joc.2225.

Sobel, A. H., E. D. Maloney, G. Bellon, and D. M. Frierson (2008), The role of surface heat fluxes in tropical intraseasonal oscillations, *Nat. Geosci.*, *1*, 653–657.

Tan, W., X. Wang, W. Wang, C. Wang, and J. Zuo (2016), Different responses of sea surface temperature in the South China Sea to various El Niño events during boreal autumn, *J. Clim.*, *29*, 1127–1142, doi:10.1175/JCLI-D-15-0338.1.

Taylor, K. E. (2001), Summarizing multiple aspects of model performance in a single diagram, *J. Geophys. Res.*, *106*(D7), 7183–7192, doi:10.1029/2000JD900719.

Toffoli, A., L. Loffredo, P. Le Roy, J. M. Lefèvre, and A. V. Babanin (2012), On the variability of sea drag in finite water depth, *J. Geophys. Res.*, *117*, C00J25, doi:10.1029/2011JC007857.

Wang, C., W. Wang, D. Wang, and Q. Wang (2006), Interannual variability of the South China Sea associated with El Niño, *J. Geophys. Res.*, *111*, C03023, doi:10.1029/2005JC003333.

Wang, D., Q. Xie, Y. Du, W. Wang, and J. Chen (2002), The 1997–1998 warm event in the South China Sea, *Chin. Sci. Bull.*, *14*, 1221–1227.

Wang, D., L. Zeng, X. Li, and P. Shi (2013), Validation of satellite-derived daily latent heat flux over the South China Sea, compared with observations and five products, *J. Atmos. Oceanic Technol.*, *30*, 1820–1832, doi:10.1175/JTECH-D-12-00153.1.

Yang, L., et al. (2015), Toward a mesoscale hydrological and marine meteorological observation network in the South China Sea, *Bull. Am. Meteorol. Soc.*, *96*, 1117–1135, doi:10.1175/BAMS-D-14-00159.1.

Yu, L., and R. A. Weller (2007), Objectively analyzed air–sea heat fluxes for the global ice-free oceans (1981–2005), *Bull. Am. Meteorol. Soc.*, *88*, 527–539, doi:10.1175/BAMS-88-4-527.

Yu, L., X. Jin, and R. A. Weller (2006), Role of net surface heat flux in seasonal variations of sea surface temperature in the tropical Atlantic Ocean, *J. Clim.*, *19*, 6153–6169, doi:10.1175/JCLI3970.1.

Zeng, L., P. Shi, W. T. Liu, and D. Wang (2009), Evaluation of a satellite-derived latent heat flux product in the South China Sea: A comparison with moored buoy data and various products, *Atmos. Res.*, *94*, 91–105.

Zeng, X., M. Zhao, and R. E. Dickinson (1998), Intercomparison of bulk aerodynamic algorithms for the computation of sea surface fluxes using TOGA COARE and TAO data, *J. Clim.*, *11*, 2628–2644.

Zhang, J. A., P. G. Black, J. R. French, and W. M. Drennan (2008), First direct measurements of enthalpy flux in the hurricane boundary layer: The CBLAST results, *Geophys. Res. Lett.*, *35*, L14813, doi:10.1029/2008GL034374.